Quantification of Local Hemodynamic Alterations Caused by Virtual Implantation of Three Commercially-Available Stents for the Treatment of Aortic Coarctation

Sung Kwon
Marquette University

Recommended Citation

Kwon, Sung, "Quantification of Local Hemodynamic Alterations Caused by Virtual Implantation of Three Commercially-Available Stents for the Treatment of Aortic Coarctation" (2013). *Master's Theses (2009 -)*. 230.
https://epublications.marquette.edu/theses_open/230

QUANTIFICATION OF LOCAL HEMODYNAMIC ALTERATIONS CAUSED BY VIRTUAL IMPLANTATION OF THREE COMMERCIALLY-AVAILABLE STENTS FOR THE TREATMENT OF AORTIC COARCTATION

by

Sung Kwon

A Thesis submitted to the Faculty of the Graduate School,
Marquette University,
in Partial Fulfillment of the Requirements for
the Degree of Master of Science

Milwaukee, Wisconsin

December 2013

ABSTRACT

QUANTIFICATION OF LOCAL HEMODYNAMIC ALTERATIONS CAUSED BY VIRTUAL IMPLANTATION OF THREE COMMERCIALLY-AVAILABLE STENTS FOR THE TREATMENT OF AORTIC COARCTATION

Sung Kwon

Marquette University, 2013

Patients with coarctation of the aorta (CoA) are prone to morbidity including atherosclerotic plaque that has been shown to correlate with altered wall shear stress (WSS) in the descending thoracic aorta (dAo). We created the first patient-specific computational fluid dynamics (CFD) model of a CoA patient treated by Palmaz stenting, and compared resulting WSS distributions to those from virtual implantation of the NumedCP and GenesisXD stents also commonly used for CoA. CFD models were created from magnetic resonance, fluoroscopy and blood pressure (BP) data. Simulations incorporated vessel deformation, downstream vascular resistance and compliance to match measured data and generate blood flow velocity and time-averaged WSS (TAWSS) results. TAWSS was quantified longitudinally and circumferentially in the stented region and dAo. While modest differences were seen in the distal portion of the stented region, marked differences were observed downstream along the posterior dAo and depended on stent type. The GenesisXD model had the least area of TAWSS values exceeding the threshold for platelet aggregation in vitro, followed by the Palmaz and NumedCP stents. Alterations in local blood flow patterns and WSS imparted on the dAo appear to depend on the type of stent implanted for CoA. These findings may aid pediatric interventional cardiologists in choosing the most appropriate stent for each patient, and ultimately reduce long-term morbidity following treatment for CoA by stenting.

ACKNOWLEDGEMENTS

Sung Kwon

I would like to sincerely thank my advisor Dr. John LaDisa for providing me with the opportunity to pursue research in cardiovascular fluid mechanics. He has helped me tirelessly with technical knowledge and guidance that led to my successfully completion of the Master’s program. I could not have asked for a better person for an advisor. I also want to thank Dr. Laura Ellwein and Dr. Lars Olson for providing support in their roles as members of my thesis committee. As a postdoctoral scholar in Dr. LaDisa's, Dr. Ellwein also shared valuable knowledge with me and the other lab members. Dr. Olson was also integral in securing the resource that allowed me and the other lab members to conduct high performance computing simulations. Without this tool, none of my research would have been possible. Lastly, I would like to thank all of my fellow CV T.E.C. lab members: Arjun Menon, Hongfeng Wang, Sara Nomeland, Tim Gundert, Andy Williams, Dave Wendell, Ronak Dholakia and DJ Quam, who helped each other like a family. The collective effort by all the members made my research easier and more enjoyable.

TABLE OF CONTENTS

LIST OF TABLES

LIST OF FIGURES

Chapter I. Introduction

1.1 Coarctation of the Aorta

Congenital heart defects, which are structural or vascular problems that arise from abnormal formation of the heart or major vessels, affects 9 out of 1000 live births, or 36,000 infants each year in the United States(1). Coarctation of the aorta (CoA) is one of the most common congenital heart defects (8-11%), and affects 5,000 to 8,000 births annually in the United States(1,2).

CoA is characterized by a stenosis of the proximal descending thoracic aorta. The stenosis is typically located just distal to the left subclavian artery, or the juxtaductal part of the aorta, which is the region where the ductus arteriosus is attached (3) as shown in Figure 1.

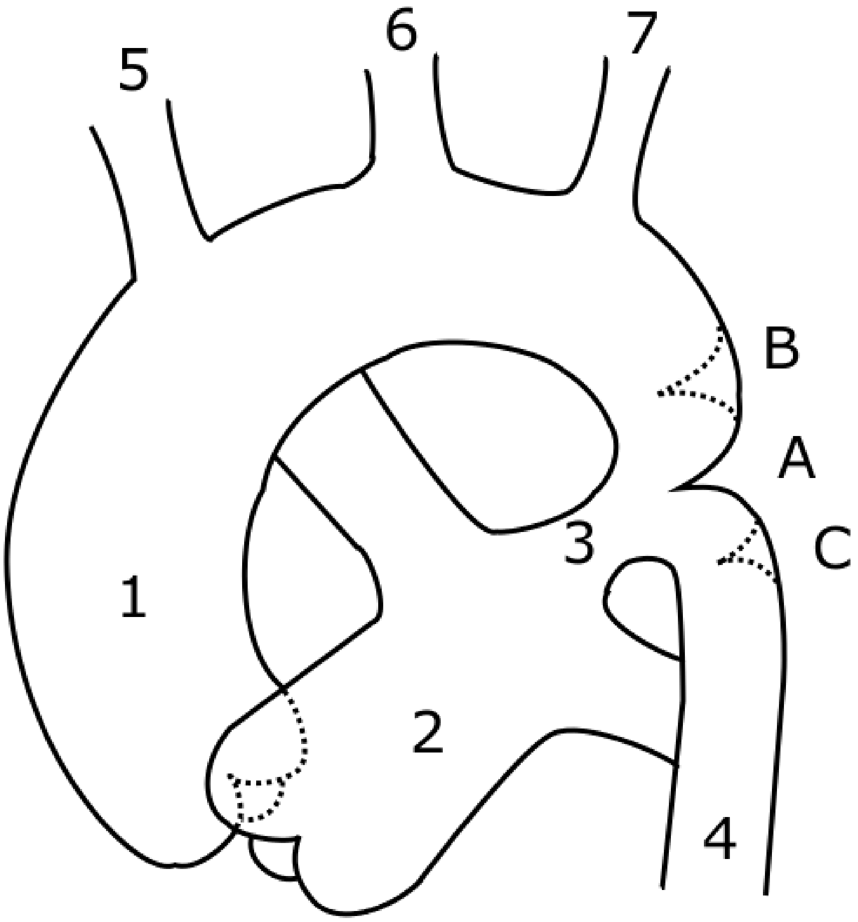

Figure 1. Diagram of the CoA location relative to other vessels.
CoA occurs just distal to head and neck vessels: A = Ductal coarctation, B = Pre-ductal coarctation, C = post-ductal coarctation. Other numbers indicate vascular regions of interest pertinent to the current investigation including 1 = ascending aorta, 2 = pulmonary artery, 3 = ductus arteriosus, 4 = descending aorta, 5 = innominate artery, 6 = left common carotid artery and 7 = left subclavian artery. Adapted from (4)

The exact mechanism on how CoA forms is still unknown. In utero, the ductus arteriosus connects the pulmonary artery and the transverse aortic arch in order to pump the blood to the descending aorta. After birth, the ductus arteriosus closes within hours or days. It is speculated that either abnormal blood flow through the ductus or extension of ductal tissue into the aorta develop aortic obstruction as the ductus closes (3). CoA can often be a cause for congestive heart failure of newborns between 2 weeks to 1 month old; however, CoA is asymptomatic in most patients and is diagnosed later in life for hypertension, murmurs or exercise intolerance. CoA can be diagnosed during a physical examination by measuring differences in upper and lower extremity blood pressure. A pressure difference of 20 mmHg is widely used as the threshold for diagnosing CoA. CoA can be also confirmed by echocardiography and magnetic resonance imaging (MRI) modalities.

1.2 Associated effects of CoA

CoA is associated with other cardiovascular defects including ventricular septal defect, atrial septal defect, aortic stenosis, mitral insufficiency, interrupted arch, and, most commonly (~80% of cases) bicuspid aortic valve. A stenosis along the aorta causes a markedly increased pressure gradient between the proximal and distal areas of the coarctation and this pressure gradient is typically measured to assess the severity of the condition. If untreated, patients are likely to develop life threatening conditions including, hypertension, cardiac dysfunction, early onset coronary artery disease, cerebral aneurysms, aortic aneurysms, aortic dissection, and stroke.

1.3 Stent implantation as a treatment method for CoA

Three main treatment options for CoA patients are surgical correction, balloon angioplasty, and stent implantation. While surgical correction has long been the mainstay of treatment, the less invasive nature, shorter hospitalization, reduced pain and decreased cost of catheter-based therapies has led to them playing an increasing role. In particular, stent implantation has become a popular choice for the ability of stents to resist recoarctation more effectively than balloon angioplasty(3).

Cardiovascular stents are used as vessel scaffolding to alleviate stenosis and restore blood flow to downstream vasculature. To date, stents have primarily been used to treat stenoses in coronary arteries, but applications of stents have extended for the treatment of peripheral arteries including the carotid, renal and femoral arteries(5). Stent implantation to treat CoA has been gaining popularity since 1991 due to its less invasive technique compared to other treatment options including surgery and balloon angioplasty. Stent implantation can avoid overdilation, dissection, and elastic recoil of the aorta, and it can promote re-growth or healing of vessel by pinning intimal flaps to the vessel wall after the intimal and medial tear(6).

Although variety of stents is used to treat CoA, off-label usage of biliary or iliac stents is typical due to the lack of Food and Drug Administration (FDA) approved stents to treat CoA. The Congenital Cardiovascular Interventional Study Consortium (CCISC) conducted a retrospective survey and found that out of 565 stent implantation procedures, 98% of them were acutely successful. Success was defined by a reduction in the ascending to descending aortic systolic blood pressure gradient to a value less than 20 mmHg immediately after the procedure. However, the long-term morbidity of stent implantation is not well known(7).

1.4 Hemodynamic alterations after stent implantation for CoA

Since the first clinical use of stents for CoA in 1991, numerous reports have shown their ability to successfully reduce the pressure gradient across a coarctation and generally restore the aorta to normal caliber(8-11). Measuring a pressure gradient across coarctation reveals whether the narrowing of the vessel has been corrected successfully in the short-term, but it must be noted that it does not evaluate the long-term impact of the stent implantation.

Although stents with various designs may satisfy the pressure gradient criteria for success, the geometry of stents used in other vascular beds is known to influence local flow disturbances(12-14) including indices of wall shear stress (WSS, defined as the tangential force per unit area exerted on a blood vessel as a result of flowing blood). LaDisa et al demonstrated that there is a positive correlation between the pattern of neointimal hyperplasia and regions with low WSS in the stented iliac arteries of rabbits(12). Wentzel et al. showed that the implantation of the stents in pig arteries causes changes in vessel geometry, which also results in deleterious alterations in WSS patterns(14).

Interestingly, the alteration of WSS in the aorta has also been linked to cardiovascular pathologies. In a study of ten middle-aged adults with pre-existing plaques, areas of low time-averaged WSS (TAWSS) were found in a rotating pattern progressing down the descending thoracic aorta (dAo) and correlated with areas of atherosclerosis(15). Other studies have indicated excessively high WSS can also be deleterious by initiating platelet aggregation(16). Thus, geometric intricacies of the particular stent used to treat CoA may uniquely influence the likelihood and severity of future dAo pathology. Stent-induced local flow alterations may also be accentuated in cases of residual narrowing where even a modest reduction in diameter within the coarctation region can accelerate blood through the stent and further contribute to deleterious downstream flow alterations. Understanding the impact of stent design on hemodynamic alterations for CoA patients will be critical to prevent long-term pathological conditions due to hemodynamic alterations in dAo. Unfortunately, no studies to date have characterized local WSS after stenting for CoA.

1.5 Patient-specific computation fluid dynamics (CFD) simulation

CFD enables detailed spatiotemporal quantification of hemodynamic indices, including WSS, using patient-specific models. CFD uses numerical methods to solve nonlinear differential equations such as the Navier-Stokes equation that describes fluid flow. Recently, CFD has been utilized for simulating blood flow in medical applications to quantify hemodynamic indices and assess their impact on vascular diseases. Advantages of using CFD over clinical data include, but are not limited to, visual capabilities, control of variables, and time and cost efficiencies. Recent improvement in medical imaging technology make it possible to perform CFD simulations based on MRI and blood pressure (BP) data instead of idealized vessels and steady flow values. This facilitates more accurate and reliable data by performing a realistic simulation of blood flow in a particular physiological region and condition of interest. The major advantage of CFD over clinical data in the current stenting research is its ability to compare the performance of a variety of stents in a single patient by incorporating stent geometry into a CFD model of the patient's vessel.

In early days of patient-specific CFD simulations, most studies were performed to elucidate the role of hemodynamic indices in the progression of atherosclerosis at the carotid and coronary arteries(17). Over the years, CFD has been used to quantify hemodynamic indices in various vasculature regions and associated diseases with advances of medical imaging technology, imaging processing, and computational capabilities. The influence of CFD has reached the field of endovascular stent design as well. In 2007, the *Virtual Intracranial Stenting Challenge* project demonstrated the reproducibility of CFD simulation techniques in patient-specific stented models of intracranial aneurysms(18).

1.6 Quantification of hemodynamic indices using CFD CoA models

Several CFD studies were conducted to understand long-term impact of CoA treatment options by quantifying hemodynamics using CoA models of various stages(19-21). Detailed patterns of altered hemodynamic indices such as WSS have also been quantified and visualized in CoA models(19). Hemodynamic alterations of CoA patients treated with resection with end-to-end anastomosis surgical repair were also evaluated through patient-specific CFD simulations. The results predicted long-term atherosclerotic plaque progression patterns in the dAo after the surgical treatment(20). Finally, Coogan et al. quantified cardiac work and compared values between stented CoA vessel and controls using CFD simulations by varying wall properties to differentiate the stented region from the rest of the aorta(21); however the detailed impact of stent design on hemodynamic alterations in dAo of CoA patients has not been evaluated using patient-specific CFD data. Quantifying hemodynamic indices in the dAo of CoA patients due to the stent implantation using patient-specific CFD simulation may ultimately provide clinicians with a tool to choose the best stent design for a specific patient based on local hemodynamic indices in the dAo. Previously, this could not be done with clinical data alone. This is an especially valuable for CoA = because there is no FDA approved stent for the condition.

1.7 Objective

Although recent findings suggest that stent implantation for CoA can alleviate a blood pressure gradient, they cannot confirm the long-term results of treatment by this approach. Altered hemodynamic indices such as WSS are known to be a cause of onset and progression of cardiovascular diseases such as atherosclerosis, thrombosis, and vessel injury. Therefore, it is important to understand the influence of stent implantation on hemodynamic indices as a surrogate for long-term morbidity after this treatment. Understanding the impact of the stent design on the long-term result can potentially aid clinicians in choosing stents with particular design that can maximize the success of the treatment.

Current medical and computing technologies allow quantification of hemodynamic indices using patient-specific CFD simulations. CFD also facilitates virtual treatment of CoA for comparison of hemodynamic alterations between stents in the same vessel. The objective of the current investigation was to create the first patient-specific CFD model of a patient treated for CoA by stenting, and compare distributions of WSS, mainly in dAo, to those resulting from virtual implantation of two other stents commonly used to treat CoA. This investigation will demonstrate the capability of current technology to assess the performance of different stent designs for CoA using patient-specific CFD simulations.

Chapter II. Methods

2.1 CFD model construction

2.1.1 Creation of patient-specific CFD models without the stent

A CFD model of the vasculature was created by converting medical imaging data into a geometrically representative computer model(22). MRI was performed for a patient previously treated for CoA by Palmaz stent placement (Cordis Corp., Miami Lakes, FL) as part of a clinically ordered imaging session and after IRB approval facilitating use of the data for computational modeling. Gadolinium-enhanced magnetic resonance angiography (MRA) was conducted to delineate vascular morphology(22,23) including the thoracic aorta, and the innominate (IA), left and right carotid (LCCA and RCCA), vertebraland left subclavian (LSA) arteries. Phase Contrast MRI (PC-MRI) was performed to calculate time-resolved volumetric blood flow(23) over the full cardiac cycle at the ascending aorta (AscAo) slightly above the aortic root (Figure 2). Upper and lower extremity supine BP were then measured using an automated sphygmometer cuff.

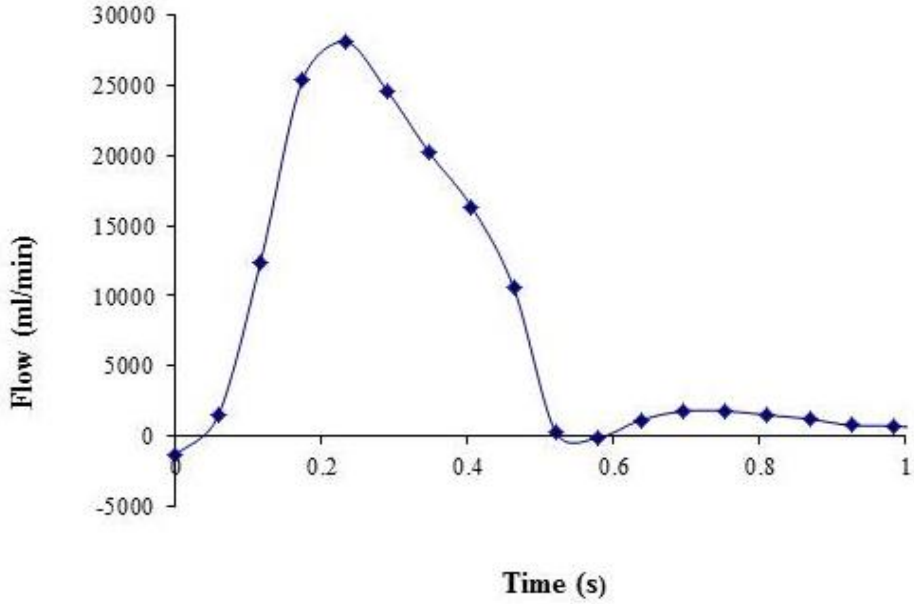

Figure 2. Time-varying blood flow calculated using PC-MRI data in the AscAo slightly above the aortic root

MRA data was processed for gradient nonlinearities(24) before CFD models were constructed using the Simvascular software package (https://simtk.org). Magnetic field inhomogeneities from the stent caused signal dropout in the volumetric MRA data (Figure 3A). Fluoroscopic angiography data from the same time period (Figure 3B) was therefore used to extract the dimensions and guide positioning of the stent within the coarctation region.

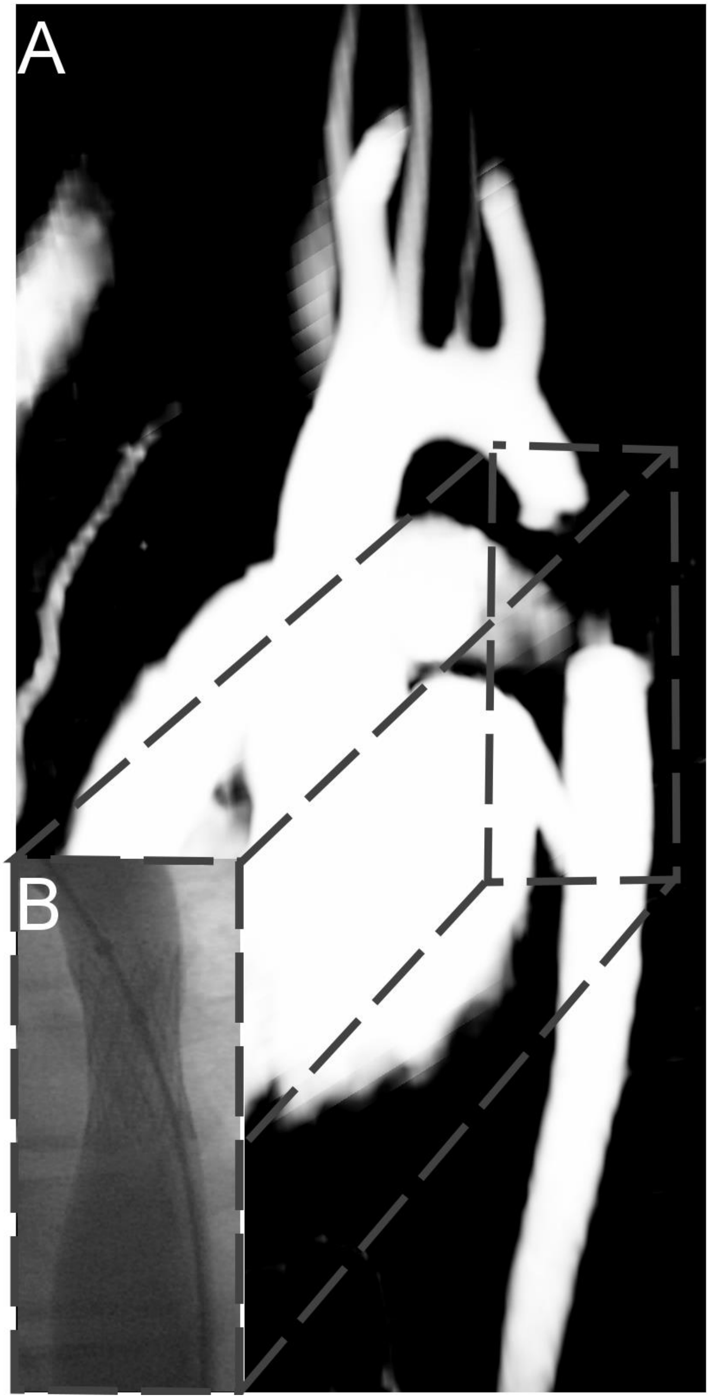

Figure 3. Mean intensity projection of MRI data (A) and an angiographic image of the same patient obtained by fluoroscopy (B).
CFD models were constructed using the MRI data with diameters of the stented region extracted from the fluoroscopy data to account for signal dropout created by artifacts due to the implanted Palmaz stent.

MRA data in DICOM image slice format was converted into 3D volume format (.vti) using eFilm (Merge Healthcare, Chicago, IL) software (Figure 4A). Simvascular was then used to find the centerline path for each vessel by manually locating spline points (Figure 4B). The lumen area along each vessel was identified by implementing automated level set and manual techniques to segment a 2D intensity window perpendicular to the paths of each vessel (Figure 4C). Dimensions extracted from fluoroscopy images were used to segment the lumen area along the stented region. 2D segments for each vessel were then lofted together to create the patient-specific CFD solid model without the stent (Figure 4D).

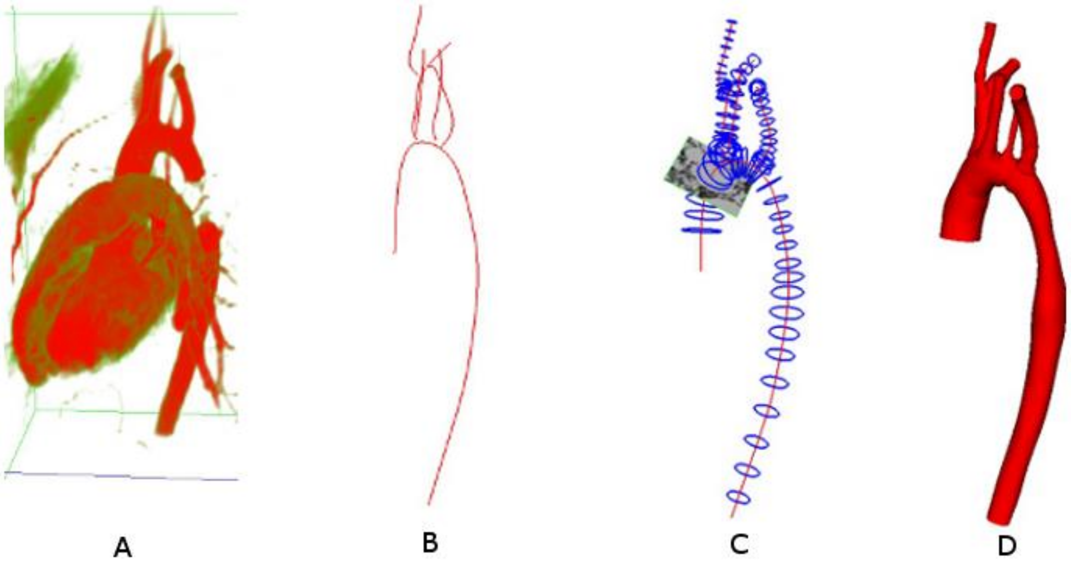

Figure 4. Creating the patient-specific CFD model.
MRA data converted to volumetric data (A). Centerline paths (B) of vessels and 2D lumen areas (C) along the vessels were segmented. A geometrically accurate patient specific CFD model (D) was then created by lofting the 2D segments of lumen areas.

2.1.2 Virtual implantation of stents

Geometric characteristics (Table 1) of the implanted and two additional stents, Numed Cheatham Platinum (Hopkinton, NY) and Genesis XD (Cordis Corp.), were obtained from literature(25,26) and the drawing of one repeating unit (Figure 5) for each stent design was created in computer aided design (CAD) software (Solidworks Corp., Concord, MA). Each version was then virtually implanted into a separate, but equivalent, CFD model of the patient's thoracic aorta before stenting using the methods described by Gundert et al(27). First, a cylinder was created with an arbitrary thickness substantially thicker than the stent's thickness, but with a length identical to the desired stents (Figure 6A). The drawing of a repeating unit of a stent, shown in Figure 5, was sketched onto a plane adjacent to the cylinder and the geometry of a stent was mapped by wrapping the plane around the cylinder (Figure 6B). The cavity of a repeating unit was proliferated longitudinally and circumferentially using the “circular” and “linear” pattern functions in CAD (Figure 6C). Protruded solids were then extracted from the remainder of the solid model to complete a thickened version of the stent (Figure 6D). The path of the aorta was imported and the thick stent was placed at the precise location of the Palmaz stent, and oriented to align with the path of the aorta (Figure 6E) using “flex” function in CAD. Solid models of the unstented aorta were then thinned to match the thickness of each stent as shown in Table 1 (Figure 6F). The intersection between versions of each “thick stent” and their corresponding thinned unstented aortic solid models created the geometrically accurate solid model of each stent (Figure 6G). These stents were then subtracted from copies of the same patient-specific computational model to produce the flow domain associated with each stent as shown in Figure 7. CFD models were then discretized into a finite element mesh as described in detail below.

Table 1. Design attributes of stents virtually implanted for CoA

	Palmaz	NumedCP	GenesisXD
Thickness (mm)	0.312	0.254	0.173
Strut width (mm)	0.338	0.300	0.205 (macro) 0.123 (micro)
Number of circumferential repeating units	14	8	11
Number of longitudinal repeating units	7	6	5
Stent/Vessel contact area (mm^2)	243	128	106

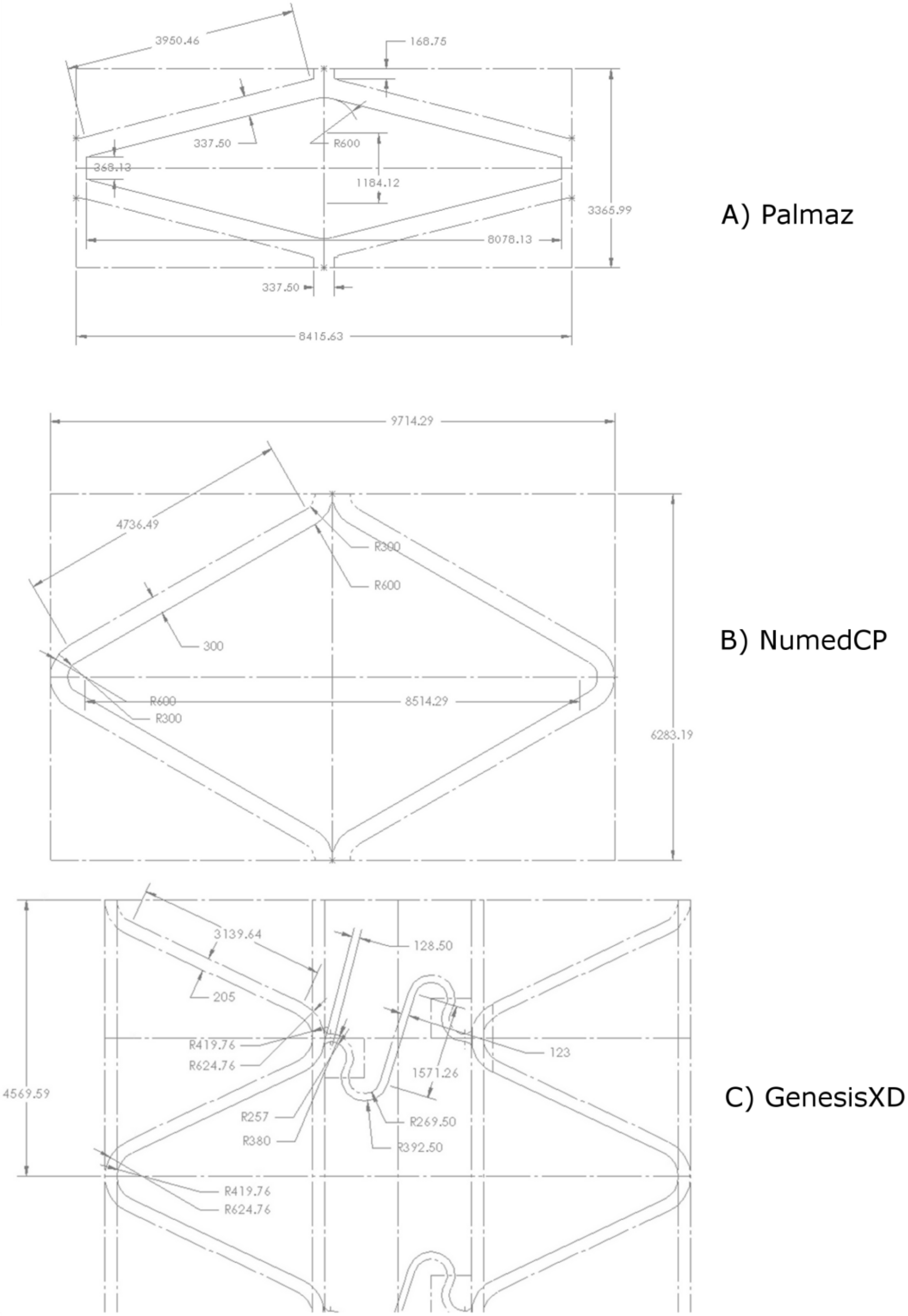

Figure 5. CAD drawings of a single repeating unit for Palmaz(A), NumedCP(B), and GenesisXD(C) stent designs with dimensions of microns.

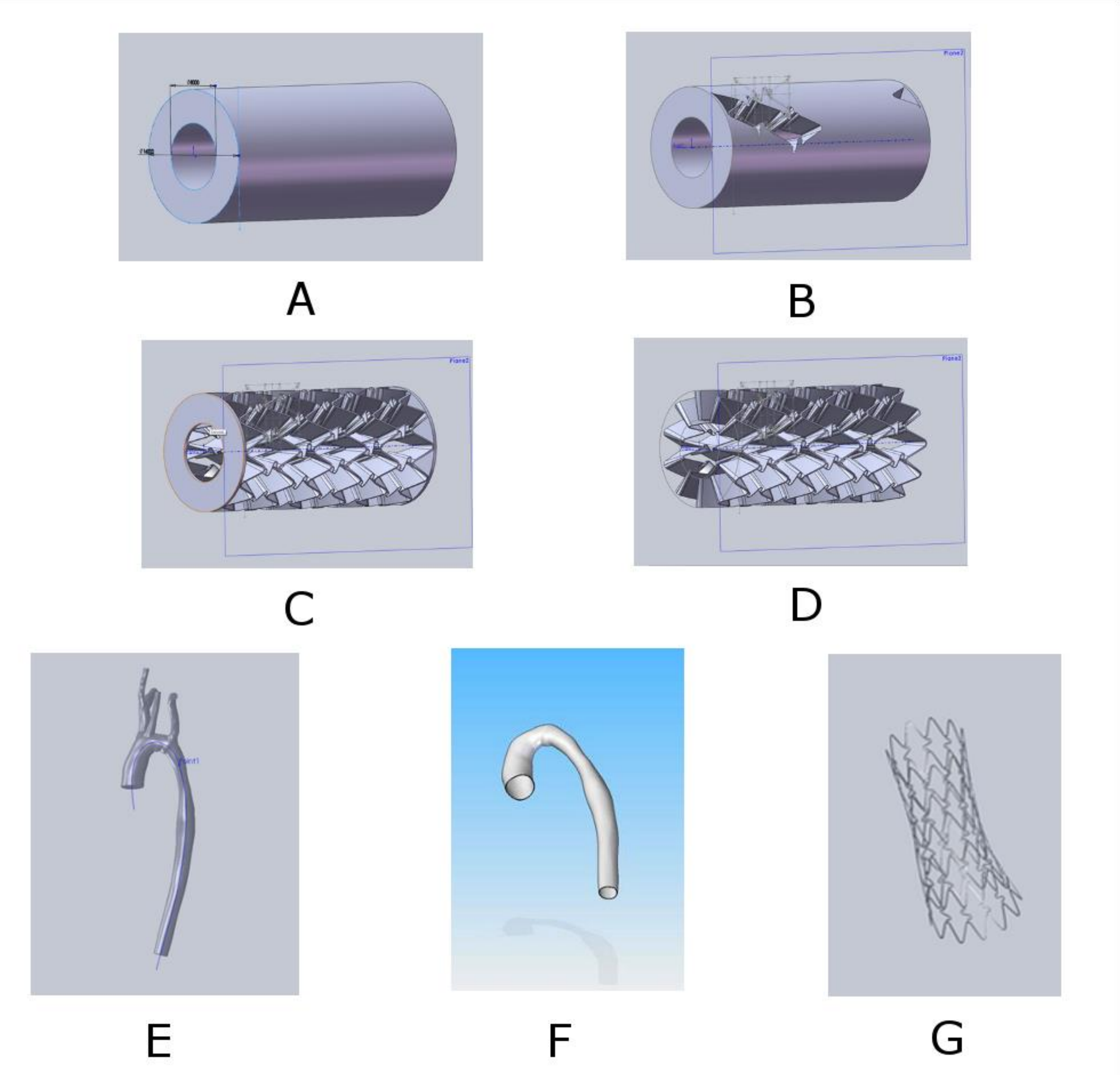

Figure 6. Solid model creation for each stent using CAD software.
A cylinder with the length identical to the stent was created (A). The geometry of a repeating unit of the stent was subtracted from the cylinder (B). The cavity of a repeating unit was proliferated linearly and circumferentially throughout the cylinder (C). Protruded solids from both sides were extracted to create athick version of the stent (D). The path of the unstented solid model was imported and the thick stent model was placed and oriented to align with the aorta (E). The unstented solid model was imported after being thinned to match the thickness of each stent (F). Intersection between the thinned unstented vessel solid model and the thick stent was conducted by a Boolean operation (G) in order to create asolid model of each stent that could then be subtracted from identical versions of the unstented patient-specific model.

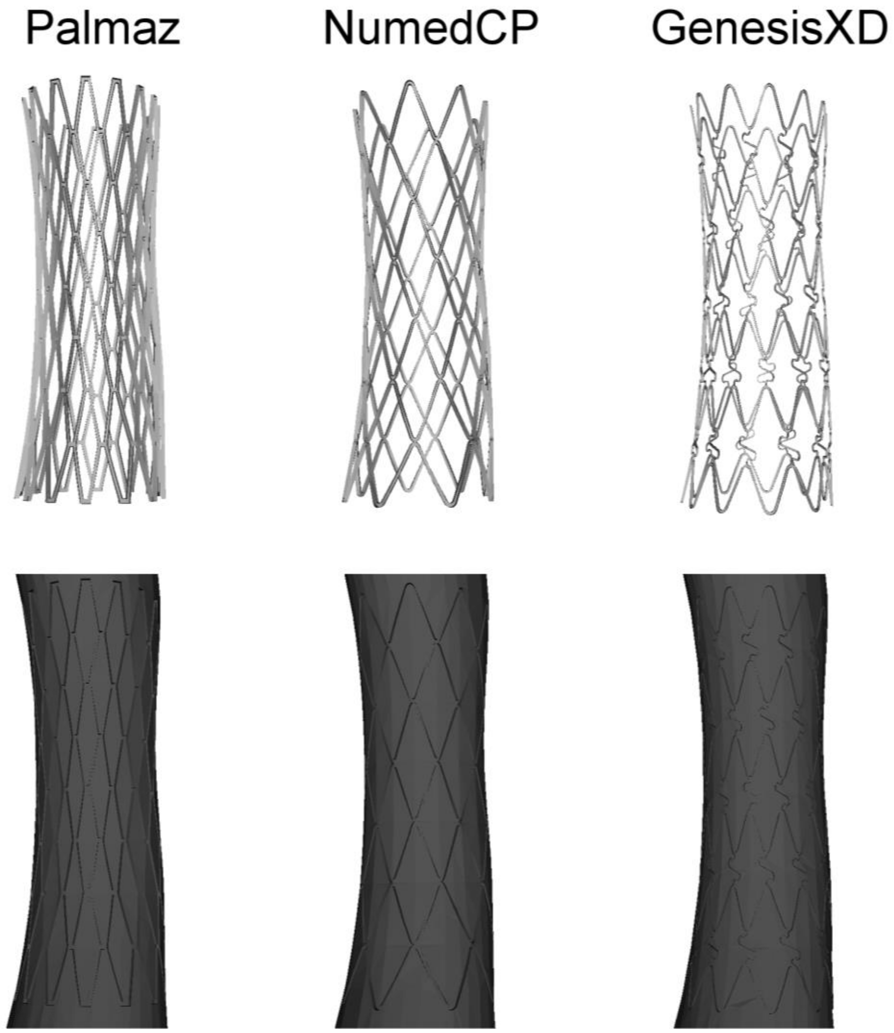

Figure 7. Flow domain associated with each stent.
Palmaz (left), NumedCP (middle) and GenesisXD (right) stents created using computer aided design software (top row). These stents were then subtracted from copies of the same patient-specific computational model to produce the flow domain associated with each stent (bottom row).

2.2 Specification of boundary conditions.

The AscAo PC-MRI waveform, as shown in Figure 2, was mapped to the inlet face of CFD models using a temporally varying plug flow profile. The distribution of blood flow to the head and neck arteries was estimated from a known relationship between their diameter and AscAo flow(28). To replicate the physiological impact of vasculature distal to CFD model branches, three-element Windkessel model outlet boundary conditions were imposed at model outlets using a coupled-multidomain method(29,30) as previously applied to CoA patients(20). Vascular wall displacement was simulated using a membrane model(31) with patient-specific elastic material properties(19), while stents were assumed to be rigid(32).

2.3 CFD simulations

Simulations were performed using a novel stabilized finite element method to solve the conservation of mass (continuity), balance of fluid momentum (Navier-Stokes) and vessel wall elastodynamics equations until the flow rate and BP fields were periodic. Newtonian and incompressible fluid assumptions were employed (4 cP and 1.06 g/cm^3, respectively) consistent with previous studies and upon consideration of shear rates in this portion of the vasculature(19,33).

2.4 Mesh Independence

Following creation, models were discretized into finite element meshes using MeshSim (Simmetrix, Clifton Park, NY). Initial anisotropic meshes corresponding to models with each stent type were refined using an adaptive method(34,35) to automatically allocate elements based on the complexity of local flow patterns and reduce computational cost as compared to isotropic meshes. While this approach allowed for appropriate edge size within proximal intrastrut regions, the adaption process uses velocity information(34,35) and hence provided less control over the number of elements in regions of low velocity within the distal portion of the stented region. Fortunately, MeshSim also allows a user to explicitly define edge lengths near a given CFD model face, such as struts or the vessel wall, through its interface within Simvascular. Smooth transitions between differences in mesh density are then created between adjacent elements regardless of their size. In order to create meshes with element sizes adequate to resolve flow features throughout the entire stent, the element size within the proximal intrastrut and stent strut regions was determined from initial adapted simulations (Figure 8) after mesh convergence, defined by less than 3% difference between TAWSS of successive meshes in the proximal intrastrut region. The numbers of elements in these initial adapted meshes were 5,149,055, 4,106,766, and 4,237,399, for the Palmaz, NumedCP and GenesisXD stents, respectively. For each stent, the three smallest elements from intrastrut areas and stented regions were extracted using ParaView (Kitware, Inc., Clifton Park, New York). Edge lengths of each extracted element were measured and the average length was calculated. Each element has four nodal points and the shortest distance between the node not located on the vessel surface plane and the vessel surface was also calculated (Figure 8). This distance is the thickness of the element and this calculation was repeated for all elements from intrastrut areas and stented regions. These dimensions (Table 2) were then assigned near stent struts as well as the vessel wall to create isotropic elements at a very high mesh density(Figure 9). The meshes created after assigning these local mesh attributes contained 3,495,606, 3,409,167 and 3,977,508 elements for the Palmaz, NumedCP and Genesis XD stents, respectively. The internal and unstented portions of meshes for each model were then adapted repeatedly until they reached ~8.3 million elements, which was adequate for similar CFD simulations(23), while the dimensions of elements in stented regions were preserved. The steps outlined above for the mesh refinement protocol that includes adaptation of an initial anisotropic mesh and adaptation of the refined meshwith specified local attributes within the stented region are summarized below for added clarity:

1. Initial anisotropic meshes for each stent were refined using an adaptive method until mesh convergence (< 3% differences in WSS between successive meshes) was achieved at the proximal stented region.

2. Edge lengths and thicknesses of elements located on the surface of the stented regions were determined based on smallest elements on the proximal stented regions of the converged meshes.

3. New initial meshes were created using the edge lengths and thicknesses of elements on the surface of stented regions.

4. Meshes were refined, except for surface elements in stented region, using an adaptive method until they reached ~8.3 million elements.

Table 2. Meshing attributes for the stented region of CFD simulations

Dimension (mm)	Palmaz	NumedCP	GenesisXD
Edge length within intrastrut area	0.144	0.135	0.120
Element thickness for intrastrut area	0.098	0.057	0.037
Edge length along stent strut	0.106	0.090	0.084
Element thickness for stent strut	0.086	0.035	0.048

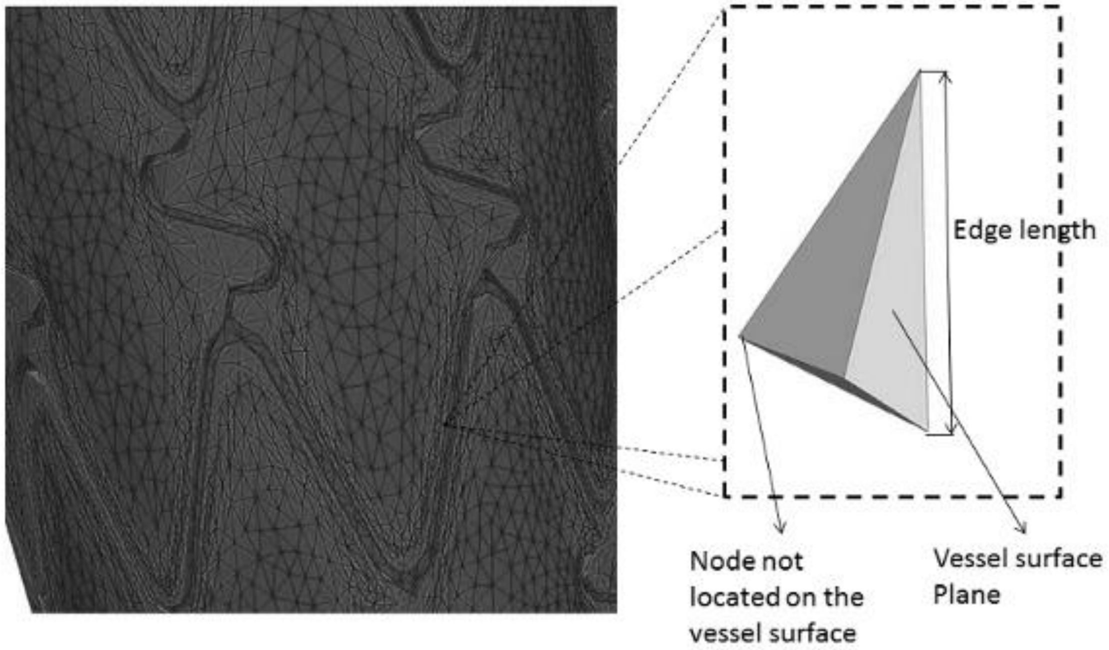

Figure 8. Estimation of the edge lengths and thicknesses of elements on the instrastrut vessel surface and stent struts.

For each stent, three surface elements from intrastrut and stented regions were extracted. The average edge lengths of the vessel surface planes were calculated. The thickness of each element was calculated by using the coordinates of three vessel surface nodes and the node not located on the vessel surface.

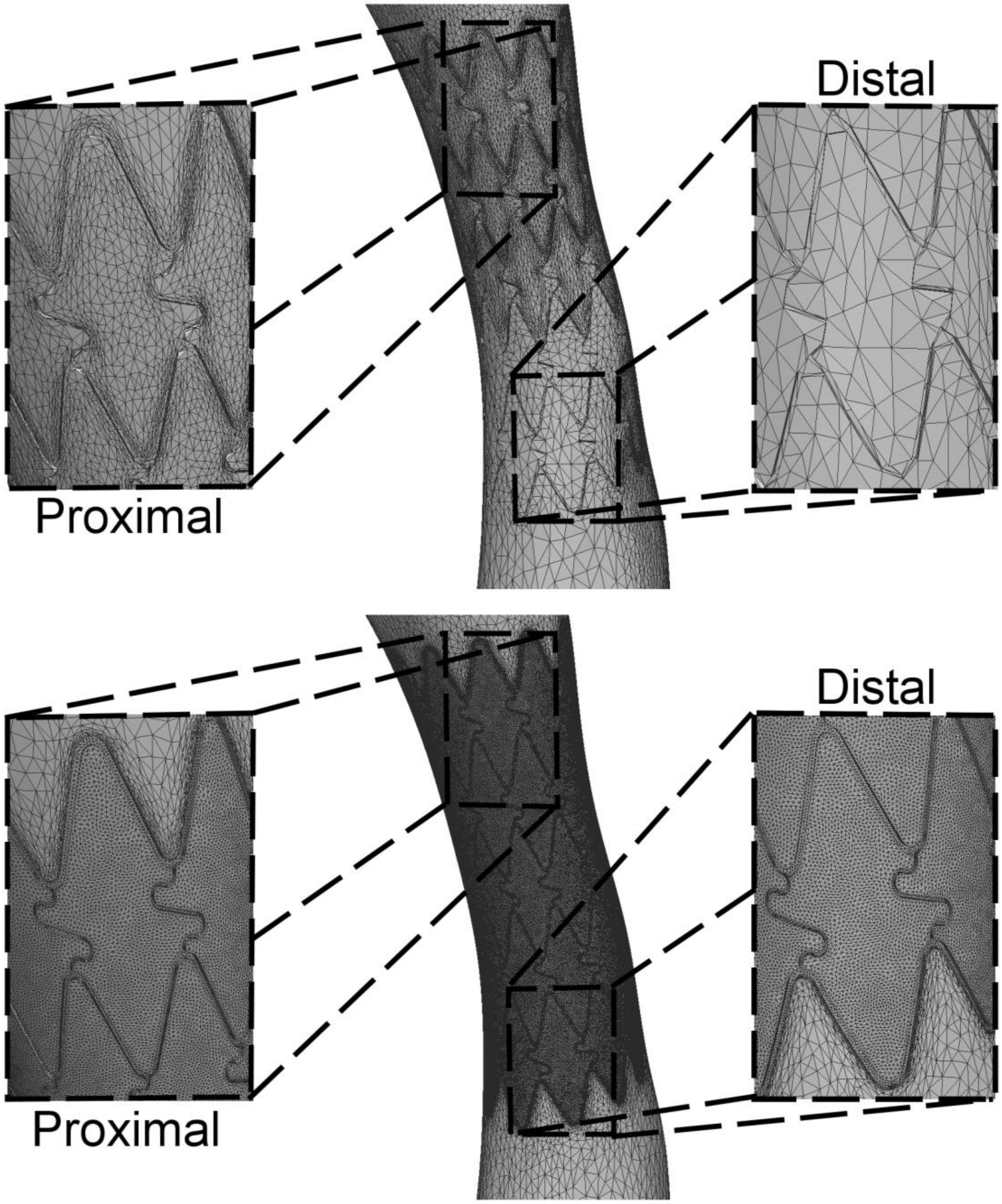

Figure 9. Image showing the meshing protocol applied for the stented region. An adaptive meshing process created elements of appropriate size in proximal intrastrut regions (A, top images), but regions of low velocity adjacent to stents struts and the distal portion of the stented region contained fewer and larger elements after the adaptive process. The minimum edge size of all elements within the proximal stented region after adapting was therefore determined and applied within the stented region for meshes containing ~8.3 million elements (B, bottom images).

To quantify the error associated with final meshes, the TAWSS results were visualized by unwrapping the surface geometry of the vessel along the inner curvature(19,33) and TAWSS indices were mapped into circumferential and longitudinal coordinates after each simulation. At the levels of proximal and distal stented regions and the dAo, TAWSS values were quantified every 0.1 degrees circumferentially by interpolating nearest TAWSS values (Figure 10). For smoother local data, each data point was filtered by 3 longitudinal points 2D moving averaging filter. Finally, TAWSS differences between successive meshes for locations in the proximal stented region were divided by TAWSS at spatially-equivalent regions, while TAWSS differences in the distal stented region with very low TAWSS were divided by average TAWSS in the dAo as reported in a prior CFD study(36).

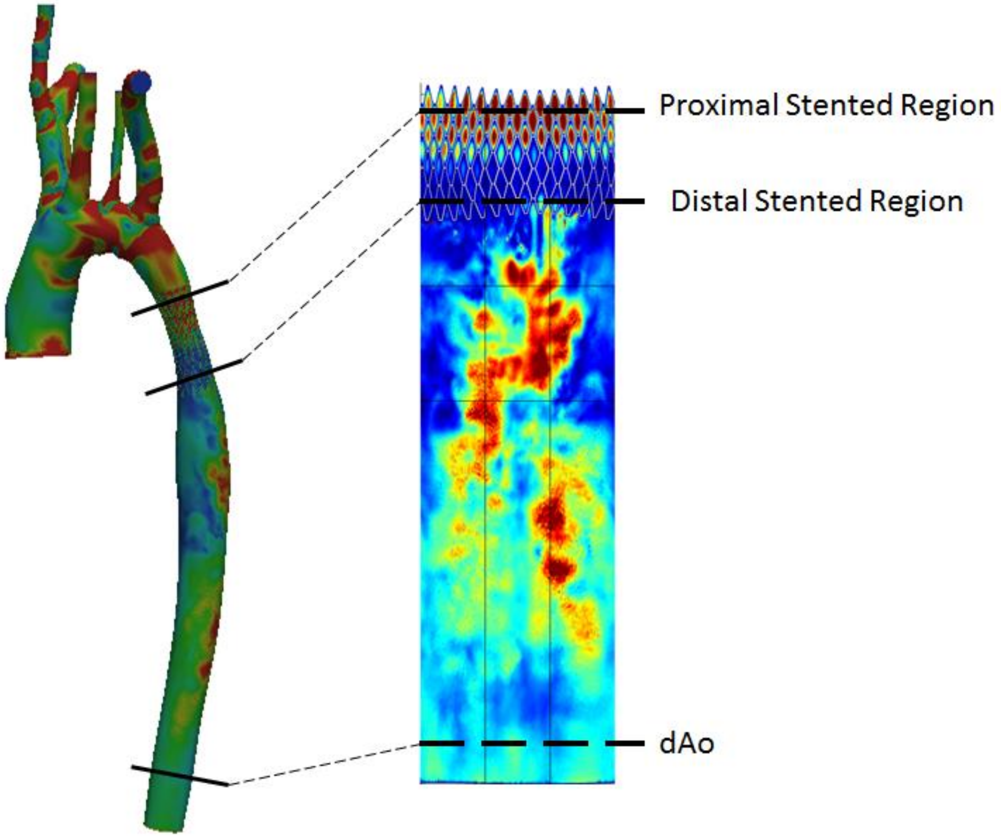

Figure 10. TAWSS quantification used for for mesh convergence calculations. After each simulation, surface geometry was unwrapped and TAWSS indices were mapped onto longitudinal and circumferential coordinates. TAWSS at proximal and distal stented regions as well as the dAo were compared between successive meshes to calculate errors for use in evaluating mesh independence.

2.5 Quantification

As described in the Section 2.4, the surface geometry of the vessel at the inner curvature and results for TAWSS within the stented region and the dAo distal to the stent are shown in Figure 11. TAWSS values were then plotted circumferentially for proximal and distal regions of the stent as well as two locations along the dAo. TAWSS values were also plotted longitudinally along regions of particular interest within the dAo. To further delineate between local differences in TAWSS due to stent type, the area of the dAo exposed to a high TAWSS threshold of 50 dyne/cm^2 at which platelet aggregation occurs *in vitro*(16) was quantified. In addition, peak and mean Reynolds numbers were calculated at the stented region for each stent. Reynolds (Re) number is used to characterize the fluid flow, such as laminar or turbulent flow. It was calculated by the equation shown below.

$$Re = \rho v D / \mu$$

ρ = density of blood

v = velocity of blood flow

D = diameter of the stented region

μ = dynamic viscosity of blood

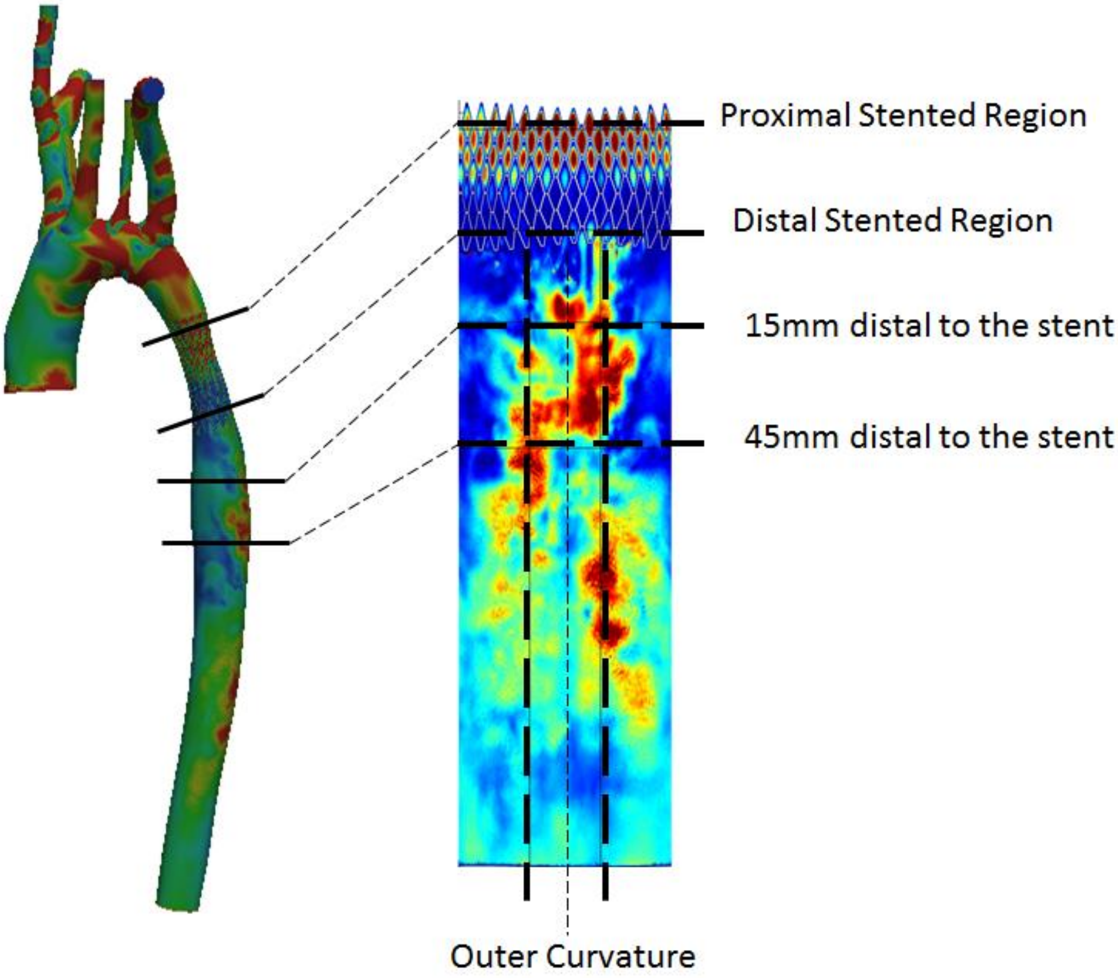

Figure 11. Approach for TAWSS quantification
TAWSS values were quantified circumferentially at proximal and distal stented regions and two locations distal to the stent, as well as longitudinally along the left and right sides of the outer curvature.

Chapter III. Results

3.1 Mesh Convergence

After all stented models were refined to reach approximately 8.3 million meshes, TAWSS errors were <9% within the stented region between the two latest meshes for each stented model. (Table 3). The circumferential average of TAWSS on the surface of dAo at 4mm upstream from the outlet of the CFD model was consistent throughout all meshes. Errors at proximal stented regions were significantly lower than those from distal stented regions. Among stented models, the Palmaz stent had the lowest errors and NumedCP stent had the largest errors. In overall, the magnitude of errors reduced as meshes were refined.

Table 3. Mesh convergence results.

Palmaz	Number of elements	TAWSS at the dAo (dyn/cm^2)	Comparison	% error at the distal stented region	% error at the proximal stented region
Mesh 1	3,495,606	N/A	N/A	N/A	N/A
Mesh 2	3,693,418	N/A	N/A	N/A	N/A
Mesh 3	4,157,478	33.3	Mesh 2 vs Mesh 3	4.40	3.44
Mesh 4	5,216,609	34.4	Mesh 3 vs Mesh 4	4.12	3.38
Mesh 5	6,251,205	33.7	Mesh 4 vs Mesh 5	2.37	2.50
Mesh 6	7,116,057	34.9	Mesh 5 vs Mesh 6	2.56	2.30
Mesh 7	8,371,221	33.7	Mesh 6 vs Mesh 7	4.04	2.10
GenesisXD		TAWSS at the dAo (dyn/cm^2)	Comparison	% error at the distal stented region	% error at the proximal stented region
Mesh 1	3,977,508	N/A	N/A	N/A	N/A
Mesh 2	4,206,059	N/A	N/A	N/A	N/A
Mesh 3	5,180,314	33.7	Mesh 2 vs Mesh 3	11.67	5.99
Mesh 4	6,223,007	33.2	Mesh 3 vs Mesh 4	8.67	4.23
Mesh 5	6,821,393	33.5	Mesh 4 vs Mesh 5	7.75	3.10
Mesh 6	8,194,977	34.6	Mesh 5 vs Mesh 6	4.60	2.78
NumedCP		TAWSS at the dAo (dyn/cm^2)		% error at the distal stented region	% error at the proximal stented region
Mesh 1	3,495,606	N/A	N/A	N/A	N/A
Mesh 2	3,693,418	N/A	N/A	N/A	N/A
Mesh 3	4,157,478	33.5	Mesh 2 vs Mesh 3	12.76	6.54
Mesh 4	5,216,609	33.0	Mesh 3 vs Mesh 4	12.07	5.17
Mesh 5	6,251,205	33.2	Mesh 4 vs Mesh 5	14.13	3.38
Mesh 6	7,116,057	33.7	Mesh 5 vs Mesh 6	11.27	3.03
Mesh 7	8,371,221	33.5	Mesh 6 vs Mesh 7	8.44	2.86

3.2 CFD simulation results

Pressure and flow results from final simulations using deformable blood vessel were compared to measured physiologic values (Table 4). Parameters in three-element Windkessel model boundary conditions were modified for each mesh so that the diastolic, systolic and pulse pressures of simulations matches the measured physiologic values.

Difference in pressure and flow in dAo between the deformable simulations and the physiological value did not exceed 5 mmHg and 6%, respectively, for all stented models. Pressure and flow between stented simulations were consistent.

Table 4. Pressure and flow differences between CFD simulation results and measured physiological values

		IA	RCCA	LCCA	LSA	Collateral	dAo (Outlet)
Palmaz	Systolic Pressure (mmHg)	1	-5	0	-1	-1	-5
	Diastolic Pressure (mmHg)	0	0	0	0	0	0
	Pulse Pressure (mmHg)	1	-5	0	-1	-1	-5
	Flow (%)	3.5	5.0	4.7	6.6	6.8	5.7
NumedCP	Systolic Pressure (mmHg)	1	-5	-1	-1	-1	-5
	Diastolic Pressure (mmHg)	0	0	0	0	0	0
	Pulse Pressure (mmHg)	1	-5	-1	-1	-1	-5
	Flow (%)	3.6	5.1	4.7	6.6	6.8	5.7
GenesisXD	Systolic Pressure (mmHg)	1	-6	-1	-2	-2	-4
	Diastolic Pressure (mmHg)	0	0	0	0	0	0
	Pulse Pressure (mmHg)	1	-6	-1	-2	-2	-4
	Flow (%)	3.3	4.8	4.5	6.3	6.5	6.0

Elevated TAWSS values (e.g. >100 dyn/cm^2) were observed within the proximal portion of the stented region and in the dAo 10 to 110 mm distal to the stent, with varying severity depending on stent type (Figure 12). The Palmaz stent showed two focal regions of elevated TAWSS in the dAo. The first initiated along the outer right luminal surface ~10 mm distal to the stent and extended to the center and then the outer left surface over ~40 mm. The second was located 75-100 mm distal to the stent along the outer right luminal surface. The NumedCP stent also displayed two focal regions of elevated TAWSS along the outer left and right luminal surfaces ~30 to 70 mm distal to the stent. In contrast, the GenesisXD stent displayed a single focal region of elevated TAWSS along center of the outer luminal surface from ~10 to 20 mm distal to the stent. The lowest TAWSS values (<25 dyn/cm^2) appeared within the distal stented region and along the inner curvature of the proximal dAo 0 to 50 mm downstream regardless of the type of stent implanted.

Circumferential quantification revealed higher TAWSS along the outer portion of the stented region (Figure 12, locations 1 and 2), while TAWSS along the inner curvature did not exceed 20 dyn/cm^2. Differences in TAWSS were more pronounced in the distal versus the proximal stented region. For example, TAWSS peaked at ~ 80 dyn/cm^2 in the distal region of the GenesisXD simulation as compared to values >80 dyn/cm^2 throughout the entire proximal stented region. The Palmaz stent had the lowest value of peak TAWSS in the distal region (51.7 dyn/cm^2) as compared to NumedCP (80.0 dyn/cm^2) and GenesisXD (82.4 dyn/cm^2). The region with elevated TAWSS ~15 mm distal to the stent (Figure 12, location 3) was also quantified circumferentially. Spatial distributions of TAWSS were similar among stents with highest values along the outer curvature (peak TAWSS of 95.7, 82.6 and 120.9 dyn/cm^2 for Palmaz, NumedCP and GenesisXD, respectively) and low TAWSS values <25 dyn/cm^2. Peak TAWSS ~45 mm distal to the stent (Figure 12, location 4) was located along the left outer luminal surface of the dAo for Palmaz and NumedCP (90.5 and 139.4 dyn/cm^{2}respectively), while the GenesisXD had a more uniform TAWSS distribution with a peak value of 64.8 dyn/cm^2 along the outer curvature.

Longitudinal quantification was additionally performed along regions of the dAo distal to the stent with elevated TAWSS. Distributions of TAWSS along the outer left luminal surface for NumedCP and Palmaz stents (Figure 12, location 5) were elevated between 20 mm and 110 mm with peak values of 168 and 110 dyn/cm^2 as compared to 49.3 dyn/cm^2 for the GenesisXD. Differences in TAWSS along the right outer luminal surface (Figure 12, location 6) were less pronounced between stents with values for GenesisXD generally lower than others.

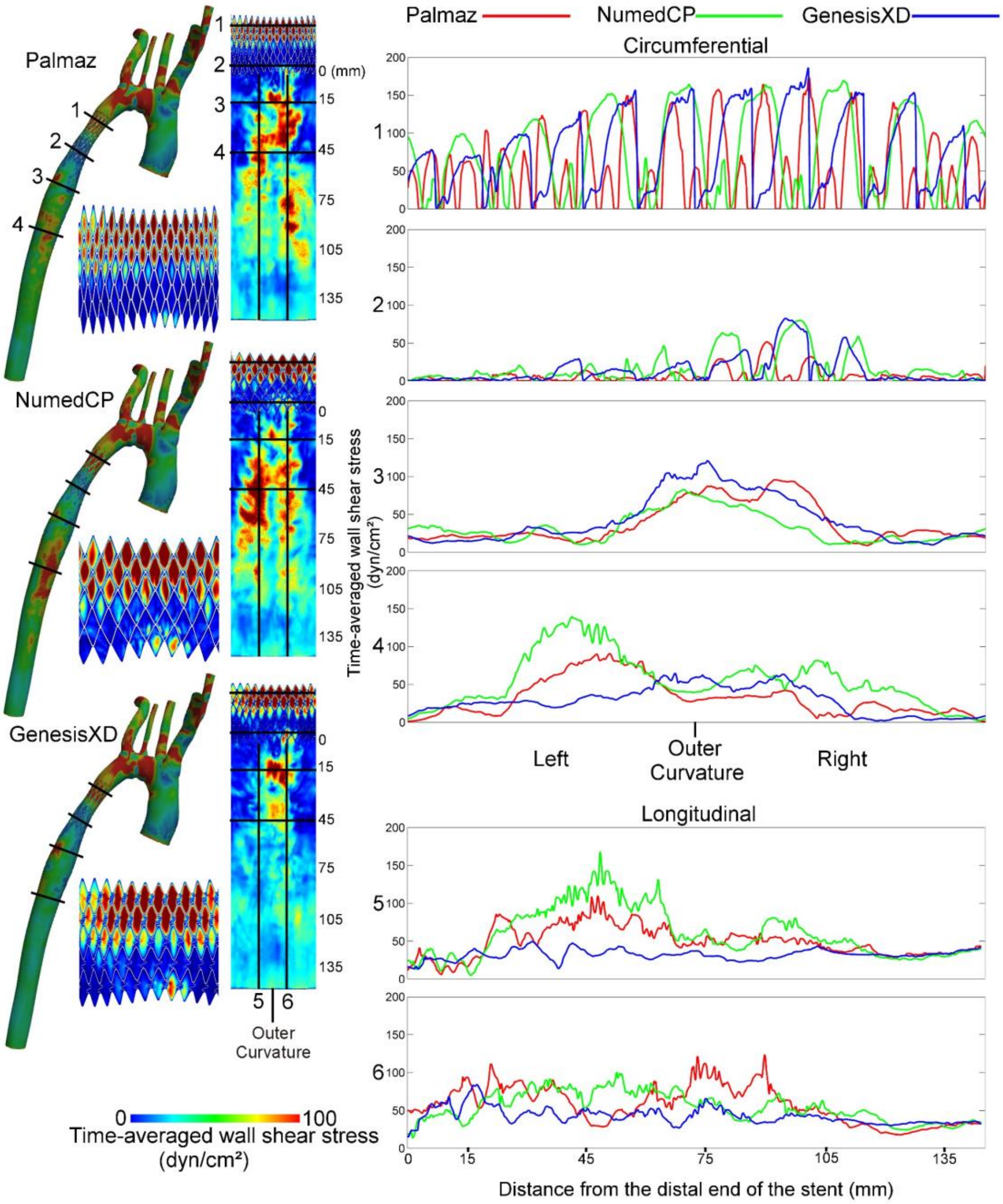

Figure 12. Distributions of time-averaged wall shear stress for the Palmaz, NumedCP, and GenesisXD stents.

CFD results for the full model are shown next to spatial maps that have been unwrapped about the outer (posterior) surface for the stented region and the distal descending aorta. Circumferential and longitudinal plots are also shown at several locations: proximal stented region (1), distal stented region (2), 15 mm distal to the stent (3), 45 mm distal to the stent (4), as well as the left (5) and right (6) portions of the outer curvature. Note that values occurring atop stent struts have been removed to improve the legibility of plots.

Figure 13 shows the area of TAWSS in the dAo exceeding the threshold for platelet aggregation *in vitro*(16). The GenesisXD model had the least area of TAWSS above the threshold (Table 5) followed by the Palmaz and NumedCP stents.

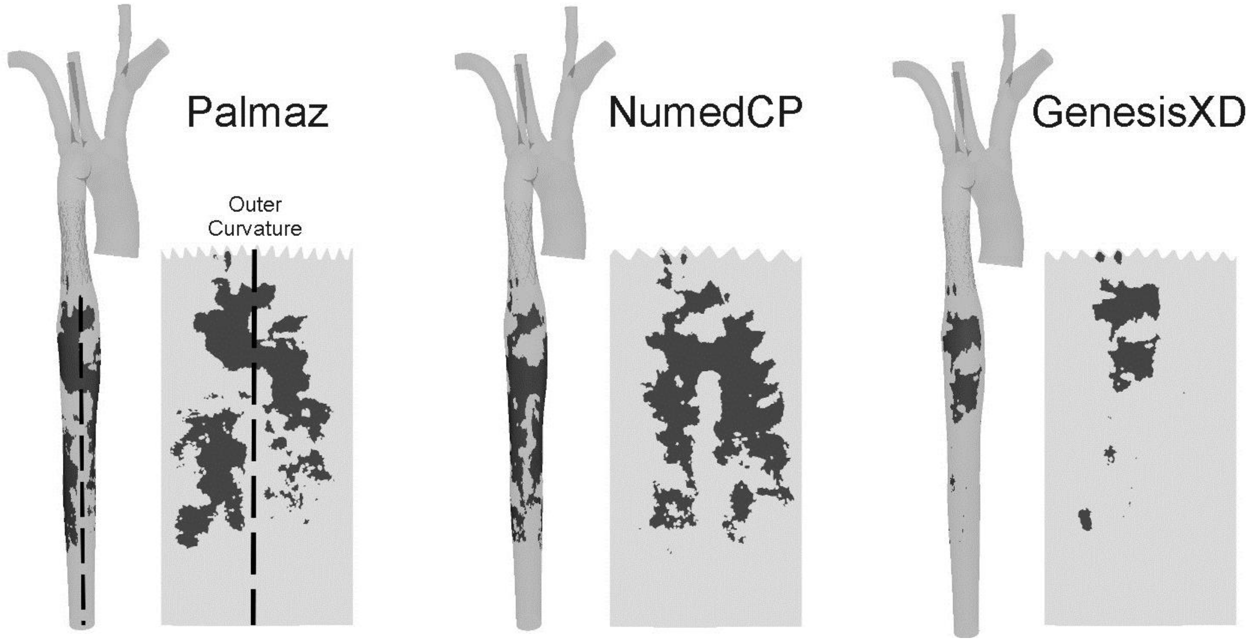

Figure 13. Locations of elevated time-averaged wall shear stress for the Palmaz, NumedCP, and GenesisXD stents.
The full CFD model results are shown next to spatial maps that have been unwrapped about the outer (posterior) surface for the descending aorta distal to the stent. Regions with time-averaged wall shear stress above 50 dyn/cm^2 have been made opaque. Values above this threshold have been previously correlated with platelet aggregation in vitro.

Table 5. The area (mm^2) of the descending thoracic luminal surface exposed time-averaged wall shear stress above the threshold for platelet aggregation in vitro

	Palmaz	NumedCP	GenesisXD
Area (mm^2) in descending aorta with TAWSS above the threshold (mm^2)	1880	2010	559

Peak and mean Re numbers from NumedCP and GenesisXD stents simulation results were compared to those from the Palmaz stent (Table 6), for further use in interpreting the findings above.

Table 6. Comparisons of peak and mean Re numbers between stents

viscosity (g/mms)	0.004
density (g/mm^3)	0.00106
stented region diameter (mm)	11.72

	Palmaz	Numed	Genesis
Peak flow (ml/min)	11047	11041	11201
Peak Re	5303	5300	5378
% diff	n/a	0.05	-1.40

	Palmaz	Numed	Genesis
Mean flow (ml/min)	3678	3677	3688
Mean Re	1766	1766	1771
% diff	n/a	0.02	-0.27

Chapter IV. Discussion

The objective of the current investigation was to create the first patient-specific CFD model of a patient treated for CoA by stenting, and compare resulting distributions of WSS in the stent and dAo to those from virtual implantation of two other stents commonly used to treat CoA. This objective was motivated by stent implantation playing an increasing role in the treatment of CoA. Since currently there are no FDA-approved stents specifically designed for children and a limited number of CoA patients at any given center, recent studies have documented several fundamental concerns regarding the use of stents in a manner other than that for which they were intended (i.e. off-label). Among these concerns is the impact of stents on hemodynamic indices including blood flow, pressure and WSS. Registries such as the Congenital Cardiovascular Interventional Study Consortium (CCISC) have been formed to obtain data pertaining to concerns such as these across multiple institutions. The current work illustrates how CFD can also provide useful insight and scrutinize stent performance in a retrospective or *a priori* manner.

The main finding of the current work is that alterations in local blood flow patterns and WSS imparted on the thoracic aorta in patients treated for CoA may uniquely depend on the type of stent implanted. While modest differences were seen in the distal portion of the stented region, marked differences were observed downstream along the posterior luminal surface of the dAo. It is important to note that the methods applied with CFD models in the current work were carefully controlled to isolate the influence of stent design. The overall vessel geometry, including residual narrowing of the vessel in the stented region, was consistent between simulations. Inlet and outlet boundary conditions were also consistent for all models, resulting in <0.3% difference in the distribution of flow to the dAo between simulations for each stent type. The current results indicate adverse local flow alterations were least severe for the GenesisXD, for which regions of elevated TAWSS and variability at the specific locations quantified were smallest. In contrast, the Palmaz and NumedCP stents both contained a greater percentage of high TAWSS along the posterior dAo. These differences are likely rooted in the design attributes intrinsic to each stent. Attributes including strut thickness, proximity, angle relative to the primary flow direction and stent:lumen area ratio were generally predictive of potentially adverse distributions of WSS in prior studies(13,37,38). Since all stent struts disturb blood flow, thicker struts protrude further into the flow domain and increase the severity of these disturbances. Similarly, the relative ratio of stent-to-vessel area influences the total amount of the vessel wall exposed to potentially deleterious flow patterns. The angle of struts relative to the primary direction of fluid flow, together with the overall stent geometry, can also influence the severity of flow disturbances caused by a stent. Stents with their linkages primarily arranged longitudinally have the potential to cause less severe flow disruptions as compared to ring-and-link designs primarily arranged circumferentially. For example, when stents are expanded to larger diameters, as can occur with redilation for recurrent CoA, their overall linkage design becomes arranged in a less longitudinal manner causing adjacent layers of fluid to be redirected more abruptly as they pass through the stented region. In contrast, larger intrastrut regions aligned in the primary direction of fluid flow limit separation and stagnation between struts. The Palmaz stent modeled in the current investigation with the greatest strut thickness and width, number of circumferential and longitudinal repeating units, and ratio of stent-to-vessel area showed two focal regions of elevated TAWSS in the dAo. The NumedCP stent with larger intrastrut area and only slightly thinner struts also displayed two focal regions of elevated TAWSS along the dAo. In contrast, the GenesisXD stent with the thinnest struts, large intrastrut regions, and ratio of stent-to-vessel area similar to the NumedCP stent displayed a single focal region of elevated TAWSS downstream of the stent.

An analysis of Reynolds numbers may further explain the current results. The Reynolds number is a dimensionless parameter describing the ratio of convective inertial forces to viscous forces. Values <2,000 constitute laminar flow where adjacent layers of fluid move in layers without mixing, while those >2,000 are characterized as turbulent or transitional. Mean and peak Re in the dAo for the patient studied here were approximately 1,750 and 5,300, respectively. These Re suggest flow was generally laminar throughout the cardiac cycle, but there were undoubtedly portions of the cardiac cycle during which flow was transitional or turbulent. During these times modest differences in local vessel geometry caused by design attributes of a particular stent could cause perturbations resulting in irregular erratic intermingling of fluid particles downstream of the stent and manifest in the differences observed.

The current results may have important clinical implications as low TAWSS values are associated with the onset and progression of cardiovascular disease in many vascular beds(39), and TAWSS above a certain preferential value may be associated endothelial injury, plaque rupture, or thrombogenesis(40,41). For example, a previous study of healthy young adults found areas of adverse WSS in a rotating pattern progressing down the dAo(42). A second previous study of ten middle-aged adults with pre-existing plaques revealed similar WSS patterns that correlated with areas of atherosclerosis(15). When joined with the results of the current investigation, the collective findings suggest the type of stent used to treat CoA may uniquely influence the location and severity of aortic plaque. In addition to vascular remodeling processes triggered by indices of WSS(43), local velocity jets and accompanying high TAWSS values imparted on the posterior wall due to a particular stent type may lead to tortuosity as seen in a rabbit model of CoA(44), or disturb the cushioning function of the thoracic aorta by increasing stiffness(45). However, these hypotheses remain to be tested in a follow-up study conducted with patients previously undergoing treatment of CoA using different stents.

While there are many publications quantifying outcomes from stenting as compared to surgery or balloon angioplasty, most of these studies have grouped outcomes from several stents together thereby resulting in a paucity of data comparing one stent type to another for metrics beyond stent fracture. To our knowledge, this is the first investigation to incorporate realistic stent geometries into an entire patient-specific thoracic aortic CFD model in order to quantify the impact of stent design on local hemodynamic alterations. While previous CFD studies involving stenting of the thoracic aorta provided invaluable information, they often included limitations such as omitting detailed geometric intricacies of a stent, used models restricted to the stented region, used idealized vessel models or did not include analysis of downstream hemodynamic alterations. The current investigation strongly suggests these downstream hemodynamic alterations unique to a given stent may be an important factor contributing to mechanical stimuli, and likely influencing vascular remodeling or plaque formation, after treatment for CoA.

The current results also extend the body of literature using CFD to study treatments for CoA by quantifying TAWSS alterations due to stent design. Previously Coogan *et al.* used a patient-specific CFD model of the thoracic aorta to study compliance mismatch created by making a portion of the dAo rigid, which had only a modest impact on cardiac work and blood pressure(21). The current results can also be appreciated relative to those from CFD models of untreated CoA patients and those corrected by end-to-end anastomosis or end-to-side repair that used methods equivalent to those employed here(19). The range of peak WSS in the dAo shown here seem to fall below the values observed with untreated patients (1,777-6,000 dyn/cm^2), but were still more severe than those observed with surgically corrected or normal patients in this previous work.

The current study should be interpreted with the constraints of several potential limitations. The strut cross section of the virtually implanted NumedCP was rectangular due to restrictions associated with the virtual stenting process, but the actual cross sectional shape of struts for this stent is circular. The use of a NumedCP stent with circular struts would likely decrease the severity of downstream hemodynamic alterations shown here. Future studies will strive to incorporate this realism. The prolapse of tissue into intrastrut regions was not considered here since the main focus was to quantify hemodynamic alterations downstream of the stented region and isolate the impact of different stent designs. Nevertheless, this factor should also be considered in future studies, perhaps using the approach Murphy *el al.* applied in CFD models of a stented coronary artery(13). Although an analysis of mesh independence showed the difference in TAWSS between successive meshes generally reduced as meshes were refined, mesh independence could not be definitively concluded, as TAWSS difference between last two Palmaz meshes increased from previous successive meshes. It is possible even finer meshes are required for mesh independence, but the desktop computers used to refine meshes in our laboratory have limited capability in their RAM and are therefore unable to create meshes with a number of elements exceeding 8.3 million. Additional mesh independence studies are needed in future work. Each stented model underwent up to 15 rigid wall simulations followed by a deformable wall simulation. Due to the large number of elements, it took approximately 2 months of computational time for each deformable simulation. Future modification of the mesh convergence strategy applied here and increased computational power may reduce the duration of future analyses. The Reynolds numbers quantified suggest that flow is transitional or turbulent during portions of the cardiac cycle. Error associated with analyzing transitional or turbulent flow using CFD software with a linear solver should be specifically quantified through comparison with results from CFD software that incorporates a turbulence model. Future studies can then implement other methods as needed to capture thenature of the transitional or turbulent flow more appropriately for future stented models of the aorta.

While the detailed patterns of TAWSS shown here are influenced by stent type, general flow patterns through the thoracic aorta are also largely dictated by vessel morphology for the patient modeled and distributions of blood flow to the head and neck arteries. For example, the presence of elevated TAWSS in the proximal stented region was a function of patient morphology and may not have been present in a patient with a gothic or crenel arch(46). Nonetheless, the current investigation demonstrates that the type of stent implanted can influence TAWSS distributions, which may be further accentuated or mitigated depending on a given patient's aortic morphology.

In summary, the current study is the first to quantify downstream hemodynamic alterations due to stenting in CoA patients using patient-specific CFD models with virtually implanted stents. The current results showed marked differences in TAWSS patterns in the downstream dAo depending on the stent implanted. Following confirmation with future studies, these findings may aid pediatric interventional cardiologists in choosing the most appropriate stent for each patient, and thereby reduce long-term morbidity following treatment for CoA by stenting.

BIBLIOGRAPHY

1. Rosamond W, Flegal K, Furie K, Go A, Greenlund K, Haase N, Hailpern SM, Ho M, Howard V, Kissela B and others. 2008. Heart disease and stroke statistics-2008 update: A Report From the American Heart Association Statistics Committee and Stroke Statistics Subcommittee. Circulation. Volume 117. United States. p e25-146.

2. Ferencz C, Rubin JD, McCarter RJ, Brenner JI, Neill CA, Perry LW, Hepner SI, Downing JW. Congenital heart disease: prevalence at livebirth. The Baltimore-Washington Infant Study. Am J Epidemiol 1985;121(1):31-6.

3. Rao P. Coarctation of Aorta. Current cardiology reports 2005;7:425-434.

4. Dholakia RJ. Numeric Modeling of Hemodynamics in the Thoracic Aorta and Alterations by Dacron Patch Treatment of Aortic Coarctation (Master's thesis): Marquette University; 2009.

5. Sniderman KW. Noncoronary vascular stenting. *Prog Cardiovasc Dis* 1996;39:141-64.

6. Bruckheimer E, Pedra C. Stenting Options for Coarctation of the Aorta. Interventional Cardiology Clinics 2013;2(1):115-129.

7. Ringel RE, Gauvreau K, Moses H, Jenkins KJ. Coarctation of the aorta stent tria (COAST): study design and rationale. Am Heart J. 2012;164(1):7-13.

8. Harrison DA, McLaughlin PR, Lazzam C, Connelly M, Benson LN. 2001.Endovascular stents in the management of coarctation of the aorta in the adolescent and adult: one year follow up. Volume 85: Heart. p 561-566.

9. Magee AG, Brzezinska-Rajszys G, Qureshi SA, Rosenthal E, Zubrzycka M, Ksiazyk J, Tynan M. 1999.Stent implantation for aortic coarctation and recoarctation. Volume 82: Heart. p 600-606.

10. Perloff JK. Coarctation of the aorta. Clinical recognition of congenital heart disease. Philadelphia: Saunders. p 113-143.

11. Redington AN, Hayes AM, Ho SY. Transcatheter stent implantation to treat aortic coarctation in infancy. Br Heart J 1993(69):80-82.

12. LaDisa JF, Jr, Olson LE, Molthen RC, Hettrick DA, Pratt PF, Hardel MD, Kersten JR, Warltier DC, Pagel PS. Alterations in wall shear stress predict sites of neointimal hyperplasia after stent implantation in rabbit iliac arteries. Am J Physiol Heart Circ Physiol 2005;288(5):H2465-H2475.

13. Murphy JB, Boyle FJ. A full-range, multi-variable, CFD-based methodology to identify abnormal near-wall hemodynamics in a stented coronary artery. Biorheology 2010;47(2):117-132.

14. Wentzel JJ, Whelan DM, van der Giessen WJ, van Beusekom HM, Andhyiswara I, Serruys PW, Slager CJ, Krams R. Coronary stent implantation changes 3-D vessel geometry and 3-D shear stress distribution. Journal of Biomechanics 2000;33(10):1287-1295.

15. Wentzel J, Corti R, Fayad Z, Wisdom P, Macaluso F, Winkelman M, Fuster V, Badimon J. Does shear stress modulate both plaque progression and regression in the thoracic aorta? Human study using serial magnetic resonance imaging. J Am Coll Cardiol 2005;45(6):846-854.

16. Hathcock JJ. 2006. Flow effects on coagulation and thrombosis. Arterioscler Thromb Vasc Biol. Volume 26. United States. p 1729-37.

17. Taylor CA, Steinman DA. Image-based modeling of blood flow and vessel wall dynamics: Applications, Methods and Future directions. Annals of Biomedical Engineering 2010;38(3):1188 - 1203.

18. Radaelli AG, Augsburger L, Cebral JR, Ohta M, Rufenacht DA, Balossino R, Benndorf G, Hose DR, Marzo A, Metcalfe R and others. Reproducibility of haemodynamical simulations in a subject-specific stented aneurysm model - A report on the Virtual Intracranial Stenting Challenge 2007. *J Biomech* 2008;41(10):2069 - 2081.

19. LaDisa JF, Jr., Figueroa CA, Vignon-Clementel IE, Kim HJ, Xiao N, Ellwein LM, Chan FP, Feinstein JA, Taylor CA. Computational simulations for aortic coarctation: representative results from a sampling of patients. J Biomech Eng 2011;133(9):091008.

20. Ladisa JF, Jr., Dholakia RJ, Figueroa CA, Vignon-Clementel IE, Chan FP, Samyn MM, Cava JR, Taylor CA, Feinstein JA. Computational Simulations Demonstrate Altered Wall Shear Stress in Aortic Coarctation Patients Treated by Resection with End-to-end Anastomosis. Congenit Heart Dis 2011.

21. Coogan JS, Chan FP, Taylor CA, Feinstein JA. Computational fluid dynamic simulations of aortic coarctation comparing the effects of surgical- and stent-based treatments on aortic compliance and ventricular workload. Catheter Cardiovasc Interv 2011;77(5):680-691.

22. Wilson N, Wang K, Dutton R, Taylor CA. A software framework for creating patient specific geometric models from medical imaging data for simulation based medical planning of vascular surgery. Lect Notes Comput Sci 2001;2208:449-456.

23. Les AS, Shadden SC, Figueroa CA, Park JM, Tedesco MM, Herfkens RJ, Dalman RL, Taylor CA. Quantification of hemodynamics in abdominal aortic aneurysms during rest and exercise using magnetic resonance imaging and computational fluid dynamics. Ann Biomed Eng 2010;38(4):1288-313.

24. Draney MT, Alley MT, Tang BT, Wilson NM, Herfkens RJ, Taylor CA. Importance of 3D Nonlinear Gradient Corrections for Quantitative Analysis of 3D MR Angiographic Data. Honolulu, HI: International Society for Magnetic Resonance in Medicine; 2002.

25. Ebeid MR. Balloon expandable stents for coarctation of the aorta: review of current status and technical considerations. Images Paediatr Cardiol 2003;15:25-41.

26. Forbes TJ, Rodriguez-Cruz E, Amin Z, Benson LN, Fagan TE, Hellenbrand WE, Latson LA, Moore P, Mullins CE, Vincent JA. The Genesis stent: A new low-profile stent for use in infants, children, and adults with congenital heart disease. Catheter Cardiovasc Interv 2003;59(3):406-14.

27. Gundert TJ, Shadden SC, Williams AR, Koo BK, Feinstein JA, Ladisa JF, Jr. A rapid and computationally inexpensive method to virtually implant current and next-generation stents into subject-specific computational fluid dynamics models. Ann Biomed Eng 2011;39(5):1423-37.

28. Zamir M, Sinclair P, Wonnacott TH. Relation between diameter and flow in major branches of the arch of the aorta. J Biomech 1992;25(11):1303-10.

29. Vignon-Clementel IE, Figueroa CA, Jansen KE, Taylor CA. Outflow boundary conditions for three-dimensional finite element modeling of blood flow and pressure in arteries. Comput. Methods Appl. Mech. Engrg. 2006;195:3776-3796.

30. Vignon-Clementel IE, Figueroa CA, Jansen KE, Taylor CA. 2010. Outflow boundary conditions for 3D simulations of non-periodic blood flow and pressure fields in deformable arteries. Comput Methods Biomech Biomed Engin. Volume 13. England. p 625-40.

31. Figueroa CA, Vignon-Clementel IE, Jansen KE, Hughes TJR, Taylor CA. A coupled momentum method for medeling blood flow in three-dimensional deformable arteries. Comput. Methods Appl. Mech. Engrg. 2006;195(41-43):5685-5706.

32. LaDisa JF, Jr., Hettrick DA, Olson LE, Guler I, Gross ER, Kress TT, Kersten JR, Warltier DC, Pagel PS. 2002. Stent implantation alters coronary artery hemodynamics and wall shear stress during maximal vasodilation. J Appl Physiol. Volume 93. United States. p 1939-46.

33. Wendell DC, Samyn MM, Cava JR, Ellwein LM, Krolikowski MM, Gandy KL, Pelech AN, Shadden SC, LaDisa JF, Jr. Including aortic valve morphology in computational fluid dynamics simulations: Initial findings and application to aortic coarctation. Med Eng Phys 2012;http://dx.doi.org/10.1016/j.medengphy.2012.07.015.

34. Muller J, Sahni O, Li X, Jansen KE, Shephard MS, Taylor CA. 2005. Anisotropic adaptive finite element method for modelling blood flow. Comput Methods Biomech Biomed Engin. Volume 8. England. p 295-305.

35. Sahni O, Muller J, Jansen KE, Shephard MS, Taylor CA. Efficient anisotropic adaptive discretization of the cardiovascular system. Comput. Methods Appl. Mech. Engrg. 2006;195(2006):5634-5655.

36. Moore JA, Steinman DA, Holdsworth DW, Ethier CR. Accuracy of Computational Hemodynamics in Complex Arterial Geometries Reconstructed from Magnetic Resonance Imaging. Annals of Biomedical Engineering 1999;27:32-41.

37. Duraiswamy N, Schoephoerster R, Moore J, Jr. Comparison of near-wall hemodynamic parameters in stented artery models. J Biomech Eng 2009;131(6):061006.

38. LaDisa JF, Jr., Olson LE, Guler I, Hettrick DA, Audi SH, Kersten JR, Warltier DC, Pagel PS. Stent design properties and deployment ratio influence indexes of wall shear stress: a three-dimensional computational fluid dynamics investigation within a normal artery. J Appl Physiol 2004;97:424-430.

39. Zarins CK, Giddens DP, Bharadvaj BK, Sottiurai VS, Mabon RF, Glagov S. Carotid bifurcation atherosclerosis. Quantitative correlation of plaque localization with flow velocity profiles and wall shear stress. Circ Res 1983;53(4):502-514.

40. Holme PA, Orvim U, Hamers MJ, Solum NO, Brosstad FR, Barstad RM, Sakariassen KS. Shear-induced platelet activation and platelet microparticle formation at blood flow conditions as in arteries with a severe stenosis. Arterioscler Thromb Vasc Biol 1997;17(4):646-53.

41. Karino T, Goldsmith H. Role of blood cell-wall interactions in thrombogenesis and atherogenesis: a microrheological study. Biorheology 1984;21(4):587-601.

42. Frydrychowicz A, Stalder AF, Russe MF, Bock J, Bauer S, Harloff A, Berger A, Langer M, Hennig J, Markl M. Three-dimensional analysis of segmental wall shear stress in the aorta by flow-sensitive four-dimensional-MRI. J Magn Reson Imaging 2009;30(1):77-84.

43. Gibbons GH, Dzau VJ. The emerging concept of vascular remodeling. N Engl J Med 1994;330(20):1431-1438.

44. Menon A, Wendell DC, Wang H, Eddinger TJ, Toth JM, Dholakia RJ, Larsen PM, Jensen ES, Ladisa JF, Jr. A coupled experimental and computational approach to quantify deleterious hemodynamics, vascular alterations, and mechanisms of long-term morbidity in response to aortic coarctation. J Pharmacol Toxicol Methods 2012;65(1):18-28.

45. O'Rourke MF, Cartmill TB. Influence of aortic coarctation on pulsatile hemodynamics in the proximal aorta. Circulation 1971;44(2):281-292.

46. Ou P, Bonnet D, Auriacombe L, Pedroni E, Balleux F, Sidi D, Mousseaux E. Late systemic hypertension and aortic arch geometry after successful repair of coarctation of the aorta. Eur Heart J 2004;25(20):1853-1859.